Compositions of carbonaceous-type asteroidal cores in the early Solar System. B. Zhang[1] (bdzhang@ucla.edu), N. L. Chabot[2], and A. E. Rubin[1] [1]Department of Earth, Planetary and Space Sciences, University California, Los Angeles, CA 90095-1567, USA. [2]Johns Hopkins University Applied Physics Laboratory, Laurel, MD 20723, USA.

Introduction: Most meteorites can be divided into two suites, carbonaceous (CC) and noncarbonaceous (NC) types, based on their distinct nucleosynthetic isotopic compositions [1-4]. The dichotomy indicates that the vast majority of meteorites originate from either NC (inner Solar System) or CC (outer Solar System) reservoirs. The two reservoirs may have been separated by the formation of Jupiter within the first million years of Solar System history [5].

The parent bodies of magmatic iron meteorites are the earliest differentiated asteroids, accreting <1 Ma after CAI formation [5, 6]. The iron-meteorite parent bodies formed earlier than chondritic asteroids. Thus, magmatic iron meteorites preserve, to an extent, the chemical and evolutionary signatures of the early Solar System. These signatures include the compositions and redox conditions of planetesimals, the distribution and behavior of trace elements, the sizes and numbers of planetesimals, core-formation processes, and impact events.

In this study, we present fractional crystallization modeling for 19 elements in iron-meteorite groups IIC, IID, IIF, IVB and the South Byron trio (SBT). The goals of this study are to estimate the bulk compositions of CC-iron cores, explore any chemical heterogeneities observed among CC and NC cores and identify potential mechanisms that may have produced such heterogeneities, investigate the processes responsible for fractionating siderophile elements within cores, and reconstruct the crystallization processes of CC cores.

Methods: Elemental concentrations of Cr, Co, Ni, Cu, Ga, As, Ru, Sb, Os, Re, Ir, Pt, and Au in irons were analyzed by instrumental neutron activation analysis (INAA). Most of the Ge and Sb data were obtained by radiochemical NAA (RNAA). For most irons, more than two replicates were used to calculate the mean composition. For those elements which were not analyzed by NAA (such as Mo, Rh, and Pd), we used data from isotope dilution (ID)- or LA-ICP-MS (laser ablation inductively coupled plasma mass spectrometry) from the literature [7-10].

We employed the recently upgraded fractional-crystallization modeling method [11] and used new parameterizations [12]. Sulfur and P concentrations, increasing over the course of crystallization in metallic melts, affect the behavior of siderophiles [13-16]. While P concentrations can be measured accurately in most iron meteorites, S is largely excluded from the solid metal and its content cannot be determined directly by iron-meteorite measurements. Iterative modeling of the siderophile-element trends in an iron-meteorite group can constrain the bulk S content of the core. The model uses small-step batch-crystallization modeling to simulate fractional crystallization and assumes that the siderophile elements in irons from a single core result from equilibrium mixing of solids crystallized from metallic liquids and solids crystallized from S-rich trapped melt [17]. We plotted siderophiles against As to fit compositional trends and model tracks.

Results: We used 6 ± 2 wt.% S and 2.2 ± 0.3 wt.% P for Group IIC. The IIC irons closely adhere to the solid track with low amounts (<10%) of trapped melt. The IIC members represent ≤30% crystallization products of the core.

Group IID has 0.5 ± 0.5 wt.% S and 1.9 ± 0.1 wt.% P. The current collection of IID irons represents ≤84% crystallization of the parent melt. Most IID irons indicate a relatively low fraction (<15%) of trapped melt.

The IIF irons can be reasonably fitted using bulk 5 ± 1 wt.% S and 0.65 ± 0.05 wt.% P. Our modeling shows that the four IIF irons represent ≤61% crystallization of the core. The core has low amounts of trapped melt (<10%).

The element vs. As trends of Group IVB can generally be fitted using 0.5 ± 0.5 wt.% S and 0.45 ± 0.02 wt.% P. IVB irons represent ≤78% crystallization of the parent melt. The IVB core generally has low amounts (<15%) of trapped melt.

The element vs. As trends of the SBT can be fitted with bulk 8 ± 2 wt.% S and 1.5 ± 0.3 wt.% P. The SBT core has the lowest amounts (<5%) of trapped melt among all CC-iron cores, but due to the small number of samples, the modeling results must be considered uncertain.

Discussion: Bulk S contents (0−8 wt.%) of the CC-iron cores are lower than those of several NC-iron cores: IC (19 wt.%) [18], IIIAB (9 ± 1 wt.%) [11], and IIAB (17 wt.%) [19], whereas the NC-iron IVA core (2.9 wt.% S) [20] is in the range of CC-iron cores. The S concentrations of the CC-iron cores are anticorrelated with the relative HSE abundances, but this anticorrelation is not observed in NC-iron cores. The general difference in bulk S content between the CC- and NC-iron cores may be related to the variability in S content among the precursors of iron-meteorite parent bodies in the CC and NC reservoirs.

The CI-normalized abundances of volatile and moderately volatile siderophiles in iron meteorites generally decrease along with the 50% condensation

temperatures (T_{50}) of the elements. The depletion of volatile siderophile elements in the CC-iron cores may have been inherited from their carbonaceous-chondrite-like precursors; differentiation and crystallization processes may have further shaped the volatile inventory.

Our models show that all CC-iron groups represent incomplete sampling of their cores. In all cases, the late crystallization products of all groups are modeled to be S-rich, but their latest crystallization products are missing. The lack of highly S-rich materials may be due to attrition in interplanetary space, high ablation rates during atmospheric passage, and more-rapid terrestrial weathering [21]. Our models also show that the current collections of the CC-iron groups are derived from either equilibrium solids or equilibrium mixing of solids and liquids instead of from nonequilibrium processes. This indicates that the CC-iron cores crystallized from well-mixed metallic melts and, hence, did not form significant dendrites or impact-induced cracks [17] that hindered global convection.

The bulk Os and Re concentrations in IIC, SBT, IIF, IID, and IVB cores are ~7×, ~15×, ~20×, ~30×, and ~55×CI, respectively. The elevated bulk concentrations of HSEs in a core are due either to the redox state of the parent body [10] (affecting the core/mantle ratio) and/or the admixture of different abundances of high-temperature refractory metal nuggets (RMNs) from the solar nebula [22, 23]. An important sign of the influence of RMNs in the parent melt of an iron-meteorite core is that its Ni- and CI-normalized abundances of HSEs vs. T_{50} would form a decreasing slope [23]. The high $(HSE/Ni)_{CI}$ values of groups IID and IVB have a slightly sloping pattern. Therefore, we interpret the high $(HSE/Ni)_{CI}$ values in the IID and IVB core as a result of the admixture of RMNs. Since CAI abundances show a highly linear relationship ($R^2 \geq 0.90$) with the HSE abundances in carbonaceous chondrites, we estimate ~20 vol.% CAIs for the precursors of the IVB and IID parent bodies. The IIF precursor has moderate amounts of CAIs, while those of the SBT and IIC have CI-chondritic amounts.

To account for the relatively high abundances of CAIs in some carbonaceous chondrites (e.g., CV and CK), Jupiter should have formed a pressure bump to trap infalling CAIs [24], and the bump occurred before the accretion of iron meteorites. By analogy to a similar model accounting for the variation in CAI abundance in carbonaceous chondrites [24], the HSE-rich IVB and IID parent asteroids likely accreted in the pressure bump close to Jupiter (Fig. 1). The IIF asteroid accreted a little farther out. The HSE-chondritic IIC and SBT cores developed within asteroids that accreted even farther out in the disk.

References: [1] Warren P.H. (2011) *EPSL 311*: 93-100. [2] Fischer-Goedde M. et al. (2018) *AJ 156*: 176-187. [3] Kruijer T.S. et al. (2020) *Nat. Astron. 4*: 32-40. [4] Trinquier A. (2007) *AJ 655*: 1179. [5] Kruijer T.S. et al. (2017) *PNAS 114*: 6712-6716. [6] Spitzer F. et al. (2021) *EPSL 576*: 117211. [7] Tornabene H.A. et al. (2020) *GCA 288*: 36-50. [8] Hilton C.D. et al. (2022) *GCA 318*: 112-125. [9] Walker R.J. et al. (2008) *GCA 73*: 2198-2216. [10] Hilton C.D. et al. (2019) *GCA 251*: 217-228. [11] Chabot N.L. & Zhang B. (2021) *MaPS 57*: 200-227. [12] Chabot N.L. et al. (2017) *MaPS 52*: 1133-1145. [13] Malvin D.J. et al. (1986) *GCA 50*: 1221-1231. [14] Chabot N.L. & Jones J.H. (2003) *MaPS 38*: 1425-1436. [15] Jones J.H. & Drake M.J. (1983) *GCA 47*: 1199-1209. [16] Willis J. & Goldstein J.I. (1982) *JGR: Solid Eath 87:* A435-A445. [17] Wasson J.T. (1999) *GCA 63*: 2875-2889. [18] Tornabene H.A. et al. (2023) *GCA 340*: 108-119. [19] Chabot N.L (2004) *GCA 68*: 3607-3618. [20] Rubin A.E. et al. (2022) *GCA 331*: 1-17. [21] Kracher A. & Wasson J.T. (1982) *GCA 46*: 2419-2426. [22] McCoy T. et al. (2019) *GCA 259*: 358-370. [23] Campbell A.J. & Humayun M. (2005) *GCA 69*: 4733-4744. [24] Desch S.J. et al. (2018) ApJS 238: 11.

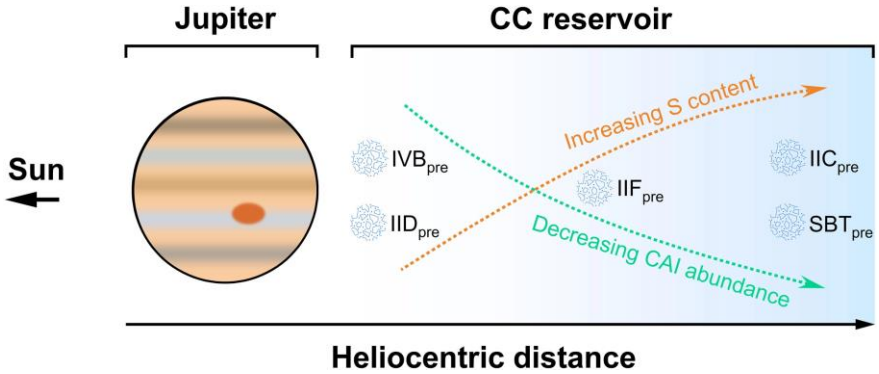

Fig. 1. Relative spatial distribution of precursors of CC-iron parent bodies.